Intrinsic photopeak efficiency measurement and simulation for pixelated CdZnTe detector

Zhuo Chen [*], Yuefeng Zhu, Zhong He

2355 Bonisteel Blvd, University of Michigan, Ann Arbor, MI, 48109, USA

ARTICLE INFO

ABSTRACT

Intrinsic photopeak efficiency of pixelated CdZnTe detectors is an important property for quantitative measurements and analysis, especially for detection and characterization of special nuclear material (SNM). The intrinsic photopeak efficiency of a single 20 mm × 20 mm × 15 mm CdZnTe detector from 59 keV to 2614 keV are measured in experiment. However, compared to the simulated ideal intrinsic photopeak efficiency, the measured efficiency showed deficit. A detailed simulation model including gamma-ray interaction physics, readout electronic as well as signal reconstruction process is built to explain this observed efficiency deficit. The simulated efficiencies of the new model match with experimental results well after taking these factors into account. Efficiency loss due to the guard ring and anode side inaccurate reconstruction are the most important factors. Other miscellaneous efficiency loss mechanisms are discussed too.

1. Introduction

The pixelated CdZnTe detectors serve as a promising alternative to High-Purity Germanium (HPGe) detectors in gamma-ray spectroscopy. Our research group at the University of Michigan has demonstrated that CdZnTe detector can achieve close to HPGe energy resolution at room temperature [1]. Detection efficiency is also of great importance as well as energy resolution. The efficiency characteristics of CdZnTe detector using IDEAS VAS/TAT system and Brookhaven National Laboratory's analog application specific integrated circuits (ASIC) have been investigated previously [2], and this work has focused on the efficiency characteristics of the latest digital ASIC-based systems. In this study, we measured the intrinsic detection efficiency of a 20 mm × 20 mm × 15 mm CdZnTe detector from 59 keV to 2614 keV and compared with simulation results. A detailed simulation package modeling the physical processes, digital readout electronics and event reconstruction has been developed to explain the mismatch between measurements and simulation, in order to diagnose the cause of the efficiency deficit.

2. Measurement of intrinsic photopeak efficiency

2.1. System overview

Two detection systems, used in the efficiency measurement experiment, are called the VAD_UM and the Orion-α system, respectively. The VAD_UM system was manufactured by Integrated Detector Electronics AS (IDEAS), and the Orion-α is developed by our research group [3].

They both can house a 3 × 3 detector array and are based on the VAD_UM v2.2 digital ASIC [3]. The dimension of CdZnTe crystals used in this study are 20 mm × 20 mm × 15 mm (Fig. 1) [1]. The anode side has 11 by 11 anode pixels with a guard ring anode surrounding them (Fig. 2). The pixel pitch is 1.72 mm between neighboring pixel anodes (Fig. 3).

When in operation, the cathode is biased to −3000 V, while the anodes are grounded. The high voltage on the cathode is provided by a high voltage generation circuit board covering the whole cathode surface. The guard ring can be biased at a small negative voltage in current system, so that events under it would be steered into the edge pixels, but this usually degrades the energy resolution of edge pixels. In this study, the guard ring was grounded to achieve best performance in energy resolution. Under this configuration, the guard ring is equi-potential with the anode pixels during operation.

The signals on the anodes and the cathode are read out by the VAD_UM v2.2 digital ASIC (Fig. 1). The digital ASIC is directly attached to the CdZnTe crystal through a carrier board by Redlen. Direct attachment yields superior noise performance as the electronic noise can be reduced to about 1.5 keV (FWHM). The energy resolution of single pixel events can reach better than 0.4% FWHM energy resolution at 661.7 keV. The ASIC samples the preamplifier output signal on electrode with a 40 MHz sampling frequency. The sampling window on each readout channel for an single pixel interaction is 4 μs and 160 samples are recorded.

---

* Corresponding author.
E-mail addresses: chzhuo@umich.edu (Z. Chen), zhuyuef@umich.edu (Y. Zhu), hezhong@umich.edu (Z. He).
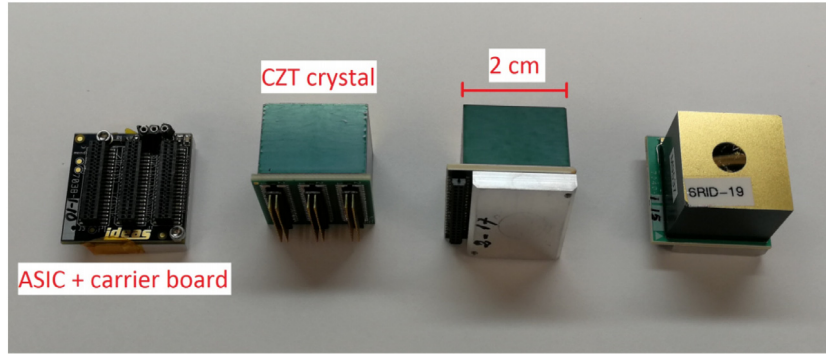
Fig. 1. From left to right, a VAD_UM v2.2 ASIC mounted on the carrier board, a 20 mm × 20 mm × 15 mm CdZnTe detector, a direct-attachment CdZnTe and ASIC module (side view) and a direct attachment detector module (top view).
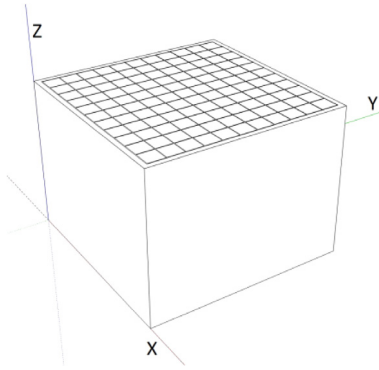

Fig. 2. Simplified scheme of a pixelated CdZnTe detector. The size of the crystal is 20 mm × 20 mm × 15 mm. One side of the crystal has 121 pixelated anodes. The other side is a planar electrode. The coordinate axis are valid throughout this study.
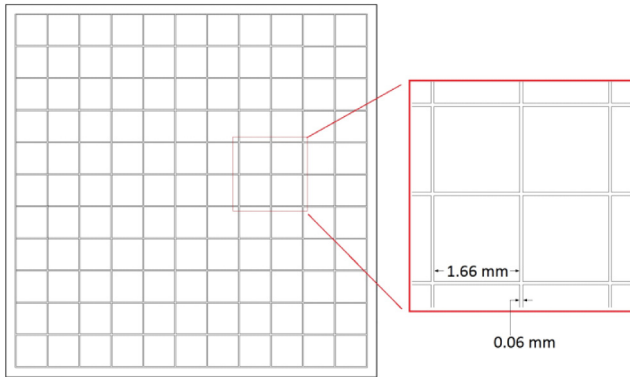

Fig. 3. Top view of the anode side of a pixelated CdZnTe detector. Each pixel pitch is 1.66 × 1.66 mm and the width of gap between two neighboring pixel is 0.06 mm.

2.2. Theory

The intrinsic photopeak efficiency of a detector primarily depends on the detector material, the radiation energy and the physical dimensions of detector [4]. The intrinsic photopeak efficiency is defined as the ratio between the number of recorded photopeak counts N_{pp} and the number of radiation quanta incident on the detector surface $N_{incident}$ [4]. The efficiency can be calculated using the following equation,

$$\epsilon_{int,pp} = \frac{N_{pp}}{N_{incident}} = \frac{N}{A \cdot B \cdot T \cdot (1 - f) \cdot \Omega} \tag{1}$$

where, N is the number of counts in the photopeak region, A is the activity of the source, Ω is the solid angle that the source sees. In far field measurement when the source is not too close to the detector, Ω can be calculated by considering the 20 mm×20 mm front area of a CdZnTe crystal,

$$\Omega = \frac{S}{4\pi d^2} = \frac{20 \text{ mm} \times 20 \text{ mm}}{4\pi d^2} \tag{2}$$

in which d is the distance between the center of the source and the upper surface of the CdZnTe crystal. The hidden assumptions are that the source is an ideal point source and emits gammas isotropically. B is the branching ratio of the photopeak emission (e.g. 85.10% for 661.7 keV of ^{137}Cs). T is the total measurement time. f is the dead time fraction of the system, and can be obtained from the firmware in our data acquisition computer program.

2.3. Experiment uncertainty analysis

The uncertainty of final efficiency result can be calculated by Eq. (3). Since T and B are known value in experiment, their uncertainty should be negligible. The elapsed time of experiment is usually long enough such that the uncertainty of N and f are very small too and therefore can be omitted in uncertainty estimation.

$$\left(\frac{\Delta\epsilon_{int,pp}}{\epsilon_{int,pp}}\right)^2 = \left(\frac{\Delta A}{A}\right)^2 + \left(\frac{\Delta\Omega}{\Omega}\right)^2 \tag{3}$$

In Eq. (3), the uncertainty of the geometry factor Ω can be calculated from Eq. (4).

$$\left(\frac{\Delta\Omega}{\Omega}\right)^2 = \left(2 \cdot \frac{\Delta d}{d}\right)^2 \tag{4}$$

According to the vendor, the labeled activity of the disk source can have an uncertainty as large as 5%. The activity of several sources are calibrated using a well-calibrated high-purity Germanium detector and the uncertainty was measured to be 2.5%. Besides, the disk source is 5 mm thick, and introduces a location uncertainty of $\Delta d = \pm 2.5$ mm.

In Eq. (1), the source is assumed to be an ideal point source and the emission of gammas is isotropic. However, the radioactive material in the disk source can be a little extended. Besides, the emission could also be anisotropic due to self-shielding. These factors are hard to model quantitatively and could cause systematic bias on the measured intrinsic photopeak efficiency.

2.4. Experimental setup

The setup of efficiency measurement is shown in Fig. 4. The source irradiates the crystal from the cathode side. It is placed 41 cm away from the detector outer case to minimize the uncertainty of source location. Even though the systems can house up to nine crystals, the intrinsic photopeak efficiency is measured separately on each individual crystals.
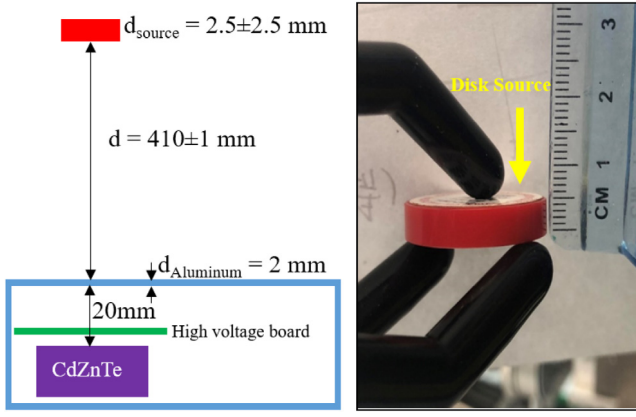
Fig. 4. (Left) The setup of the efficiency measurement experiment. The cathode side of the crystal is facing up. (Right) The sealed disk source that is used in the experiment. The thickness is 5 mm.
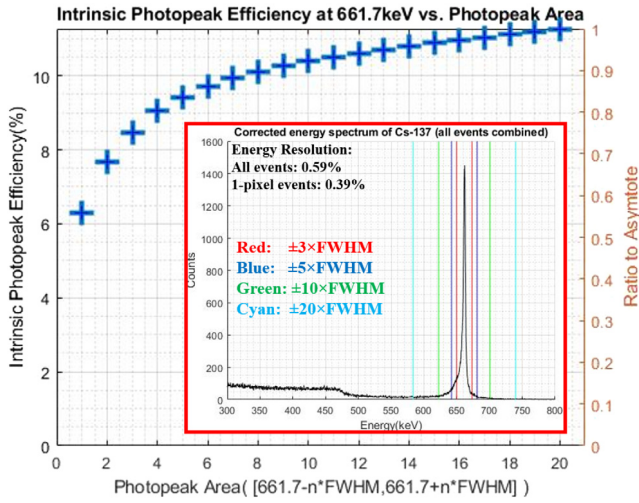

Fig. 5. (Big) Photopeak efficiency as a function of photopeak region. The orange axis on the right indicates the ratio between intrinsic photopeak efficiency and the asymptote. (Small) Measured spectrum of a ^{137}Cs source and different energy windows to define the photopeak region (Red: $\pm 3 \cdot$ FWHM; Blue: $\pm 5 \cdot$ FWHM; Green: $\pm 10 \cdot$ FWHM; Cyan: $\pm 20 \cdot$ FWHM). (For interpretation of the references to color in this figure legend, the reader is referred to the web version of this article.)

2.5. Definition of photopeak region

In experiment, the measured efficiency is highly dependent on how the photopeak region is defined. Fig. 5 shows the photopeak of ^{137}Cs (all collected events combined). Even though the energy resolution of the photopeak is superior (0.56% for all events and 0.39% for single pixel events), it is challenging to set a clear boundary to define the photopeak region. The significant low energy tail of the photopeak results from multiple factors, including charge leak, charge sharing and weighting potential cross talk (WPCT). When a narrow energy window is used, the measured efficiency is lower since some of the full-energy deposition events in the shoulders are lost. A wider photopeak region can increase photopeak efficiency, but will degrade resolving power of gamma-ray lines in real-world applications, especially when multiple characteristic gamma-ray peaks are close to each other. The photopeak region used when measuring photopeak intrinsic efficiency at different energies are shown in Table 1.

Table 1
Measured, Ideal and simulated Intrinsic Photopeak Efficiency of a single crystal at Different Energies.

Source	Photopeak Range	ϵ_{exp}	ϵ_{ideal}	ϵ_{sim}
^{241}Am (59 keV)	55–70 keV	79.98%	90.97%	81.96%
^{152}Eu (121 keV)	115–135 keV	75.74%	90.66%	80.68%
^{137}Cs (662 keV)	600–700 keV	10.81%	14.01%	11.46%
^{22}Na (1274 keV)	1190–1350 keV	4.18%	5.68%	4.35%
^{228}Th (2614 keV)	2550–2800 keV	1.35%	2.12%	1.41%

Table 2
Measured Intrinsic Photopeak Efficiency of a single crystal at 661.7 keV on two systems.

Triggering Mode	VAD_UM	Orion-α
Trigger Only	$10.69 \pm 0.43\%$	$10.79 \pm 0.31\%$
Trigger + 4	$10.70 \pm 0.43\%$	$10.82 \pm 0.32\%$
Trigger + 8	$10.64 \pm 0.43\%$	$10.81 \pm 0.32\%$

2.6. Results

The intrinsic photopeak efficiencies of a single CdZnTe crystal (ID number 6RID-23) whose size is 20 mm × 20 mm × 15 mm are measured on Orion-α system with ^{241}Am, ^{152}Eu, ^{137}Cs, ^{22}Na and ^{228}Th. When measuring the intrinsic photopeak efficiency at low energy, the high voltage board (Fig. 4) was removed to minimize gamma-ray attenuation. The measured intrinsic photopeak efficiency at different energies are summarized in Table 1.

In Table 1, ϵ_{exp} represents the measured intrinsic photopeak efficiency of a single 20 mm × 20 mm × 15 mm CdZnTe crystal. ϵ_{ideal} represents the intrinsic photopeak efficiency under ideal condition, where only the physics of gamma interaction with CdZnTe was considered. The signal induction, collection are perfect and algorithms reconstruct every event without any error. At low energy range, around 12% discrepancy between ideal efficiency ϵ_{ideal} and experiment ϵ_{exp} is observed. At 662 keV, such discrepancy becomes 23% and at 2614 keV, it is almost 40%. As energy goes higher, the discrepancy becomes more significant. This is known as the efficiency deficit problem. ϵ_{sim} represents the intrinsic photopeak efficiency after taking the actual physical processes, readout electronic and event reconstruction into account. ϵ_{sim} will be elaborated in the following section.

^{137}Cs source is used to benchmark the simulation program, so the intrinsic photopeak efficiency at 661.7 keV are measured on two systems with different crystals and different triggering modes. Introduction on different triggering modes can be found in the Ref. [3]. The efficiency of a crystal (ID number 6RID-56) was measured on VAD_UM system. The efficiency of a crystal (ID number 6RID-23) inside Orion-α was measured. The measured intrinsic photopeak efficiency performance at 661.7 keV on this two different systems are summarized in Table 2.

3. Modeling of the detection system

To explain the efficiency deficit, actual signal induction, charge collection and signal processing are included in the system modeling. A custom simulation software was developed to model the detection system.

3.1. Electron–hole pair generation

When a gamma particle incidents with the CdZnTe crystal, it may undergo Compton scattering, photoelectric absorption or pair production and transfers energy to the electrons [4]. The primary electrons produced in these processes will travel through the crystal and generate secondary electrons through ionization and excitation. As the secondary electron leaves their original site, a vacancy is also created (called a hole). Such physic process are simulated using GEANT4 10.04 package [5]. The program tracks the electron ionization process and energy
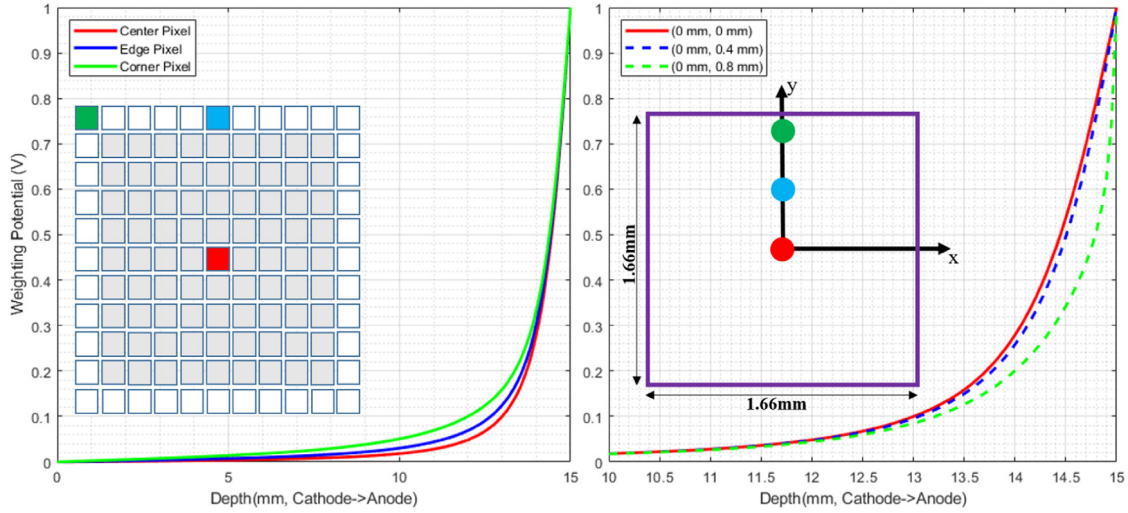
Fig. 6. The simulated weighting potential in a 15 mm thick CdZnTe crystal. In both figures, the cathode is at 0 mm and anode is at 15 mm. (Left) for pixels at different locations, the weighting potential under the pixel center show variations. (Right) for one pixel, the weighting potential at different sub-pixel location show variations. To better visualize the difference, only the weighting potential near anode side are shown.

deposition along the track. The electronic PCB, detector chamber and the system housing are modeled in the simulation. The total signal induced by the whole charge clouds on electrodes can be simulated through a superposition of the signals induced by all carriers in the charge cloud [6].

3.2. Signal induction on electrodes

The signal induction on electrodes is calculated using the Shockley–Ramo Theorem [7]. The Shockley–Ramo Theorem states that in a charge-sensitive device, the current i induced on an electrode from the movement of a point charge q can be calculated by

$$i = q\vec{v} \cdot \vec{E}_0(\vec{x}) \tag{5}$$

in which $\vec{v}$ is the instantaneous velocity of the point charge. $\vec{E}_0(\vec{x})$ is the weighting electric field at the charge location $\vec{x}$. The integral form of Eq. (5) is,

$$Q = -q \cdot \Delta\phi_0 = -q \cdot (\phi_0(\vec{x}_1) - \phi_0(\vec{x}_0)) \tag{6}$$

in which $\phi_0(\vec{x})$ is the weighting potential when the point charge is at location $\vec{x}$. Given the drift trajectory of the charge carrier from the initial position $\vec{x}_0(t)$ to the final position $\vec{x}_1(t)$, the induced signal $Q(t)$ on any electrode can be simulated.

The weighting potential can be calculated by solving the Poisson equations when only the electrode of interest is set be unit potential and all other to be zero potential, and with all spatial charge removed. Numerically, the weighting potential can be solved using Finite Element Method (FEM) with ANSYS Maxwell 18.1 software. A 20 mm × 20 mm × 15 mm CdZnTe crystal with pixelated anodes is built in software and simulated. The weighting potential of one anode pixel is sampled with a spatial resolution of 20 μm×20 μm×50 μm. The simulated weighting potential of different pixels and at different sub-pixel locations are shown in Fig. 6. As shown, the weighting potential starts to show significant subpixel variation when it is around 1.5 mm away from the anode.

Previous simulation study on analog-ASIC-based readout system assumed the weighting potential under one pixel is identical [2]. The weighting potential profile under the center of the anode pixel was selected to represent the weighting potential profile of all pixels. However, the weighting potential of central pixels, edge pixels and corner pixels do show some variations, as shown in Fig. 6 (left). Besides, the weighting potential under one pixel could also have slight lateral variations, as shown in Fig. 6 (right). For the latest system based on

the digital ASIC (VAD_UM v2.2), the collected signal pulse waveform carries richer information. Therefore, The weighting potential variation among different pixels and at different sub-pixel positions should be taken into consideration to better model the detector response.

3.3. Drift trajectory of electron–hole pairs

To simulate the transient signal on electrodes, the drift trajectory $\vec{x}(t)$ also needs to be determined. Assuming the drift of electron–hole pairs only depends on their mobility and local electric field, and the material is ideal, the drift velocity can be expressed as,

$$\begin{cases} \frac{dx}{dt} = -\mu_e \cdot E_x(x, y) = -\mu_e \cdot \frac{\partial V(x,y)}{\partial x} \\ \frac{dy}{dt} = -\mu_e \cdot E_y(x, y) = -\mu_e \cdot \frac{\partial V(x,y)}{\partial y} \end{cases} \tag{7}$$

Eq. (7) can be re-written into finite difference form, which is Eq. (8),

$$\begin{cases} \frac{x^{n+1}-x^n}{\Delta t} = -\mu_e \cdot \frac{V(x^n+\Delta x, y^n)-V(x^n, y^n)}{\Delta x} \\ \frac{y^{n+1}-y^n}{\Delta t} = -\mu_e \cdot \frac{V(x^n, y^n+\Delta y)-V(x^n, y^n)}{\Delta y} \end{cases} \tag{8}$$

in which $V(x, y)$ is the operating electric potential when the detector is biased. From Eq. (8), the location of electron (x^{n+1}, y^{n+1}) at time step n+1 can be updated from previous location (x^n, y^n),

$$\begin{cases} x^{n+1} = x^n - \mu_e \cdot \Delta t \cdot \frac{V(x^n+\Delta x, y^n)-V(x^n, y^n)}{\Delta x} \\ y^{n+1} = y^n - \mu_e \cdot \Delta t \cdot \frac{V(x^n, y^n+\Delta y)-V(x^n, y^n)}{\Delta y} \end{cases} \tag{9}$$

The actual operating field $V(x, y)$ is simulated with ANSYS Maxwell 18.1 software with actual electrode configurations (Fig. 7).

In operation, the electric field in most volume of the detector is uniform. For those electrons and holes that are right under one pixel, they will drift perpendicularly to their corresponding electrodes. However, for those electrons and holes that are generated under the gaps between pixels, the drift behavior is different. The drift electric field becomes non-uniform under the gap in near anode region. As shown in Figs. 7 and 8, when the charged particle is more than 0.05 mm away from anodes, the electric field is still quite uniform. But when it is less than 0.05 mm away from anodes, the electric field is no longer perpendicular and has some tangential components.

With $\Delta t = 0.02$ ns, $\mu_e = 75$ mm^2/V ms and $\Delta x = 1$ μm, the drift trajectory of an electron is solved and shown in Fig. 8.
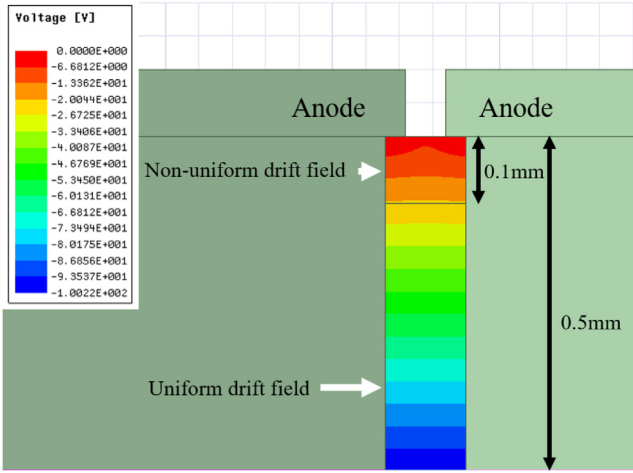
Fig. 7. The drift electric field between pixels becomes non-uniform in near-anode region. Since in deeper depth, the electric field is very uniform, only the field near the anode side is shown.
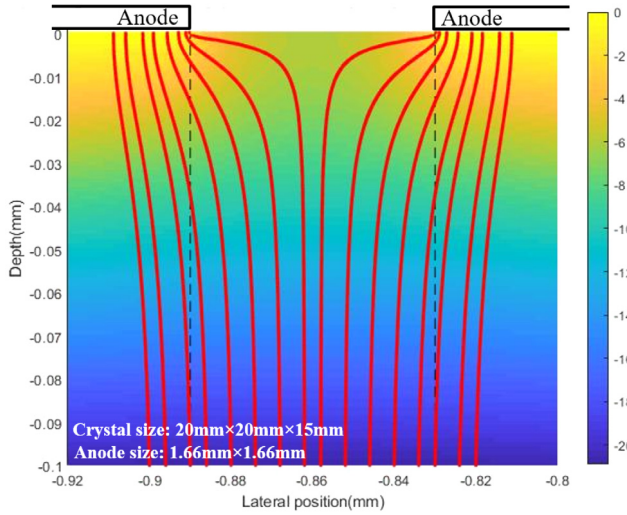

Fig. 8. The background shows the operating electric field near anode side. The red curves show the drift trajectories of several electrons that are generated at different locations under the gap. Since in deeper depth, the trajectory is straight due to uniform electric field, only the trajectory near the anode side is shown. The color bar on the right indicates the operating electric potential (Unit: Volt). (For interpretation of the references to color in this figure legend, the reader is referred to the web version of this article.)

Two phenomenons are observed from the drift trajectory simulation. First, the non-uniform electric field under the gap will bend the drift trajectory only when the electron is very close to the anode (<50 μm). In most of the detector volume, electrons and holes do drift perpendicularly to their corresponding electrodes. Second, the electrons under the gap will eventually be collected by its closest anode. These are the drift behaviors of a charge carrier under ideal condition. In actual CdZnTe crystal, the drift behavior can be more complicated and is influenced by several other effects (charge trapping, pixel-jumping effects, non-uniform electric field inside crystal, etc.). The simulation should be viewed as an close approximation to the actual case.

With the simulated drift trajectory of charge carrier and weighting potential on all electrodes, the induced transient pulse waveform on every electrode can be simulated and recorded for event reconstruction. In simulation computer program, calculating the track of each individual electron and hole is computation-intensive and unnecessary. When the electrons or holes are more than 0.05 mm away from the anodes,

they drift perpendicularly to the electrode. They will be steered into the closest anode when they are 0.05 mm away from the anodes, and the tail amplitude is then determined.

3.4. Other factors

Some other factors are also included in the model. (1) The diffusion of electron clouds are taken into account [8]. (2) The drift of holes are included in the model too. The mobility of holes are assumed to be 100 times smaller than electrons [9]. (3) A 2 keV equivalent white noise was added into the simulated waveform. (4) A 18 keV software threshold was added to determine whether a pixel has real signal or just noise. This same threshold is used in experiment. (5) The surrounding materials are included in the GEANT4 simulation program.

Electron and hole trapping are not included. Since their impact on detection efficiency is negligible [2].

3.5. Event reconstruction

The simulated waveform are processed in the same way as experimental waveform. The position and energy of a radiation event is reconstructed by our actual data processing algorithms. Detailed elaboration of event reconstruction algorithms can be found in Refs. [10, 11].

4. Efficiency loss mechanisms

After considering the signal induction and event reconstruction, the simulated intrinsic photopeak efficiency ϵ_{sim} at different energies are summarized in Table 1. In simulation, the photopeak region is defined in the same way as in experiment (Table 1). As shown, they agree very well with the measured intrinsic photopeak efficiency in experiment.

At 661.7 keV, the simulated intrinsic photopeak efficiency is $11.46 \pm 0.02\%$ while the measured one is $10.80 \pm 0.31\%$. Considering the uncertainty from experiment, there is still slight difference. The remaining discrepancy could come from the non-isotropic gamma emission from the source itself. Or the radioactive material inside the disk source cannot be simplified as a point source, and self-shielding can make the actual activity of source less than its labeled one. Such systematic error is hard to model quantitatively.

From simulation, the position distribution of the lost full-energy event can be extracted. An event is defined as "lost" if this event deposited all of its initial energy in the detector but the reconstructed energy is out of the photopeak region. The position distribution of the lost single pixel full-energy deposition events in ^{137}Cs simulation are shown as density map. Fig. 9 (left) shows the position distribution in X–Y plane. Fig. 9 (right) shows the position distribution in X–Z plane. Since any full-energy deposition that happened under the gap is a charge sharing event and will trigger two pixels, they are not included in Fig. 9. This results in dark strips between pixels in the density map.

Several mechanisms that can cause efficiency deficit are revealed and are elaborated in the following sections.

4.1. The guard ring loss

For a single CdZnTe crystal in Orion-α system, the guard ring, covering around 11.1% of the total 20 mm × 20 mm front area, is equi-potential with pixelated anodes during operation to achieve better energy resolution. Electron–hole pairs generated under the guard ring region will not be steered towards the edge anode pixels, but will end up with being collected by the guard ring. Since this region is effectively not contributing to photopeak events detection, intrinsic efficiency deficit is observed under it, as shown in Fig. 9(left). The guard ring loss is the dominant mechanism in low energy region. Most low-energy interactions happen near the cathode side and only triggers
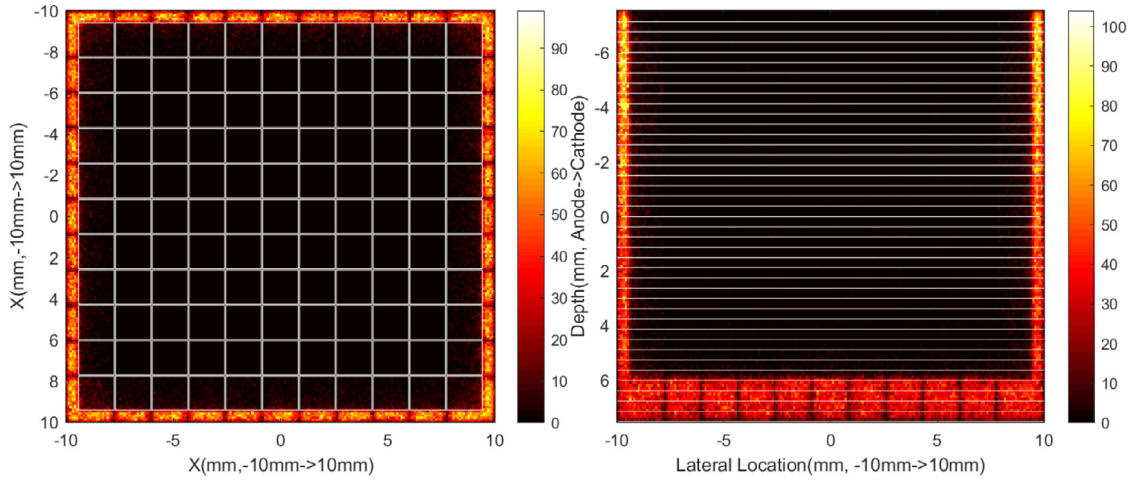
Fig. 9. The location distribution of the lost single-pixel full-energy events from simulation (661.7 keV of ^{137}Cs). (Left) the lateral position distribution. The pixel grids are marked in white for reference. (Right) a cross sectional view of the position distribution. The white lines mark the 40 depth bins.

one anode pixel. The guard ring causes around 12% efficiency loss was observed at 59 keV (^{241}Am), as shown in Table 1.

A single large crystal is more appealing in terms of efficiency if compared to several smaller crystals. For a single large crystal, there is only one large guard ring (assuming identical width) surrounding all pixels and it effectively covers less fraction of the total front area. The guard ring covers around 5% of the total front area for a larger 40 mm × 40 mm × 15 mm crystal. The guard ring loss will therefore be reduced by half and the efficiency performance should be better.

4.2. The anode side loss

Simulation and experiment also reveal the efficiency loss near the anodes. As shown in Fig. 9 (right), full-energy events are lost near the anode side.

In current event reconstruction algorithm, the material under an anode is uniformly partitioned into 40 artificial bins. Depth bin No.1 is the anode side and depth bin No.40 is the cathode side. All events in the same voxel are reconstructed with the same set of calibration parameters [10]. The weighting potential shows significant variations on both lateral and depth directions in depth bins near the anode. On the one hand, since the weighting potential changes drastically in depth direction within one depth bin, a full-energy events that happens at different depth within same depth bin can induce a signal with very different amplitude on the collecting anode. The lateral variation, on the other hand, results in different signal amplitude even though two interactions with same energy deposition happen at the same depth. Such variation in weighting potential near anode side can cause two problems in detector calibration and reconstruction, which could lead to a failed reconstruction for full-energy deposition event.

First, in the first several depth bins near anodes, the recorded photopeak is so broad that the photopeak centroid cannot be identified (see Fig. 10). Therefore, the depth-correction in calibration stage will fail since the gain at this depth is unavailable from calibration data. In Fig. 9 (right), most of the lost full-energy event near anode side are within the first four depth bins (roughly 1.5 mm thick).

Second, in the next few depth bins, even though the peak centroid can be identified from the broad photopeak in calibration stage, the reconstruction always yields broad photopeaks that extend below 600 keV. Even though the photopeak region is defined to be very wide, some full-energy events could still be lost. This explains the few scattered lost full-energy events beyond depth bin #5. Since the corner pixels have a different weighting potential profile, slightly more loss are observed under them.
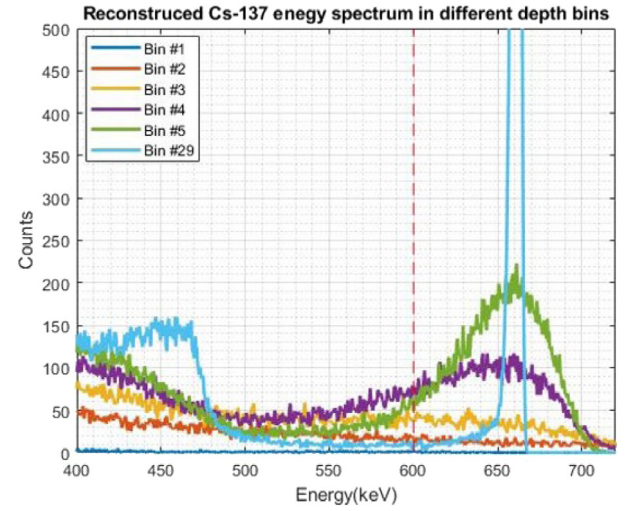

Fig. 10. The broad photopeak near anode side after calibration (experiment). Bin #1 to Bin #5 is close to anode. Bin #29 is far away from anode and is shown here for comparison.

It should be noted that such loss does not mean a 1.5 mm dead layer exists near anode. Even if one event happens in this region, it can still trigger the readout electronic and can still have a chance being correctly reconstructed into the photopeak region (see Fig. 10).

Another effect that could cause efficiency loss near anode side is the dead layer on anode side. If one event happens very shallow in the crystal on the anode side, the induced signal on anode may be too small to trigger the readout electronics. Due to the superior noise performance in direct-attachment configuration, such dead layer is estimated to be very thin and therefore is just a minor efficiency loss mechanism.

Thicker crystal is preferable in terms of detection efficiency, not only because thicker crystal is better at absorbing incident gammas, but also because in thicker crystal, the small pixel effect is more significant. The steep change of weighting potential will only happen in depth bins that are very close to the anodes. Therefore, such bad reconstruction layer on anode side will be relatively thinner in thicker crystals. The loss due to anode side bad reconstruction should be less in thicker crystals .
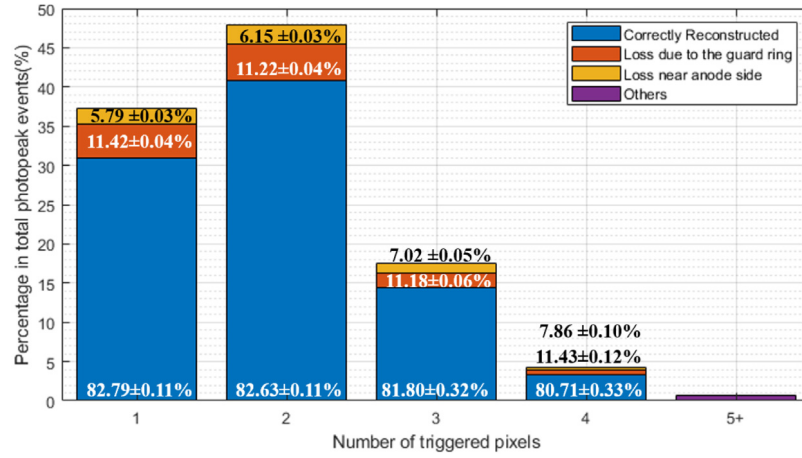
Fig. 11. The significance of loss mechanisms for different types of events at 661.7 keV (from ^{137}Cs).
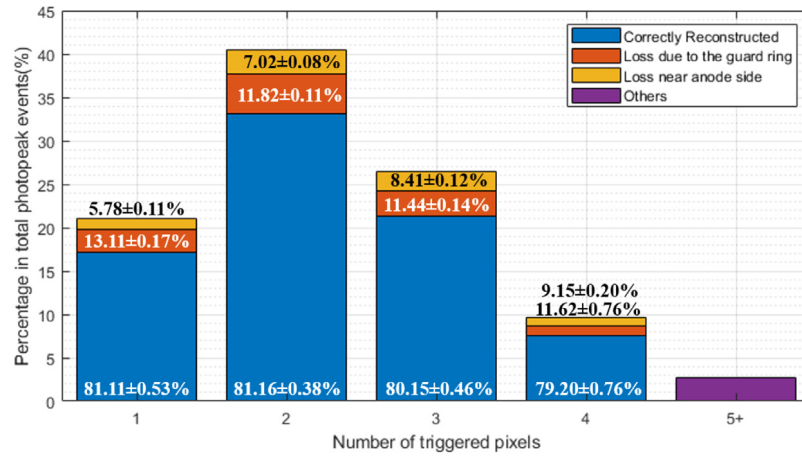

Fig. 12. The significance of loss mechanisms for different types of events at 1274 keV (from ^{22}Na).
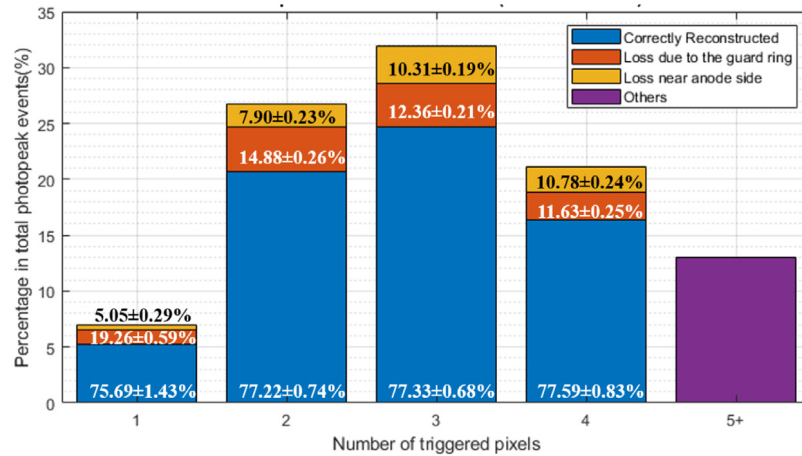

Fig. 13. The significance of loss mechanisms for different types of events at 2614 keV (from ^{228}Th).

4.3. Miscellaneous loss

At 662 keV, only around 0.75% of full energy deposition will trigger five or more pixels so in typical experiments, the waveform of these events are not recorded nor processed. However, at higher energy, much more events will trigger five or more pixels during readout. The Orion-α system does have the capability to record and process these multi-pixel events. In this study, to keep consistency, such feature was

not enabled. If detection efficiency is a critical design consideration in higher energy, the system should be designed to record and reconstruct these events, otherwise significant fraction of full-energy events would be lost.

Attenuation from surrounding materials can also degrade the intrinsic photopeak efficiency. This is negligible at 661.7 keV or higher energy since the photons in this energy range are very penetrating. But the attenuation can cause significant efficiency loss at low energy
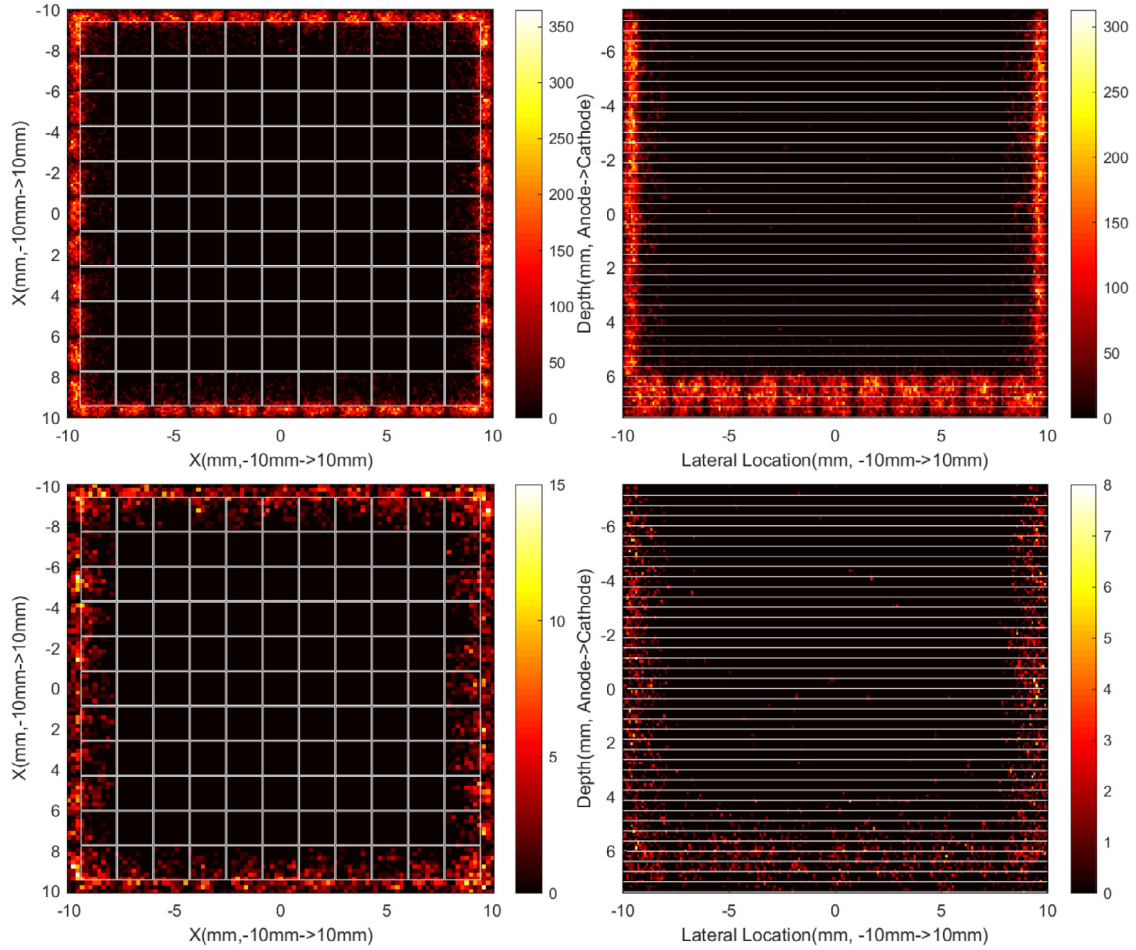
Fig. 14. The location distribution of the lost single-pixel full-energy events from simulation. Top row is at 1274 keV. Bottom row is at 2614 keV. In each row, the lateral position distribution is shown on the left. The pixel grids are marked in white for reference. The cross sectional view of the position distribution is shown on the right. The white lines mark the 40 depth bins.

range. For the 59 keV peak from ^{241}Am, the intrinsic photopeak efficiency on a single 20 mm × 20 mm × 15 mm CdZnTe detector is 79.98% without the high-voltage PCB board (Fig. 4), and reduces to 60.15% with the PCB covering the cathode. If the intrinsic photopeak efficiency at low energy region is a critical design consideration, the attenuation material between the source and crystal should be minimized.

5. Efficiency deficit analysis

5.1. Efficiency deficit breakdown

In lower energy range, most interaction are cathode side single-pixel events. Therefore, the guard ring loss is the dominant mechanism. Since the guard ring covers 11.11% of total front area, around 12% loss was observed between experimental and ideal efficiency in Table 1. In higher energy range, multiple mechanisms can cause efficiency loss. The significance of each loss mechanisms at higher energies are summarized in Figs. 11–13.

As the incident energy increases, more events would trigger five or more pixels (the rightmost bar in Figs. 11–13), which are discarded during data acquisition. Therefore, this mechanism becomes more significant.

5.2. Loss analysis on single-pixel events

The location distribution of the lost single-pixel full-energy events from simulation are shown in Figs. 9 and 14.

For single pixel events at different energies, the loss due to the guard ring shows obvious increase. At 661.7 keV, it is 11.42% and it increases to 19.29% at 2614 keV. Figs. 9 and 14 show that, as the energy goes higher, the effective width of the guard ring "dead" region is expanding due to the increased size of electron clouds. At 2614 keV, the electron cloud size can be about 1.5 mm [10]. At 2614 keV, even if one photoelectric absorption event happens under the center of the edge pixel, it can still be influenced by the "dead" region since some electrons in its electron cloud are under the guard ring and therefore are lost during signal induction.

For single pixel events at different energies, the loss near the anode surface increases as the energy deposition increases. This trend also results from the increased electron cloud size. But such loss is less rapid if compared to the loss under the guard ring loss.

5.3. Loss analysis on multi-pixel events

The analysis on multi-pixel events are based on the analysis of two-pixel events. The location distribution of the lost two-pixel full-energy events from simulation are shown in Fig. 15. If a two-pixel event is outside the photopeak region, the locations of both interactions are shown in Fig. 15 as the scattered events inside the crystal. The loss is from the same mechanisms discussed before.

For two-pixel events at different energies, the loss due to the guard ring and near anode side both increase as energy increases. The major reason is that the effective dead region is expanding due to the increased size of the electron cloud.
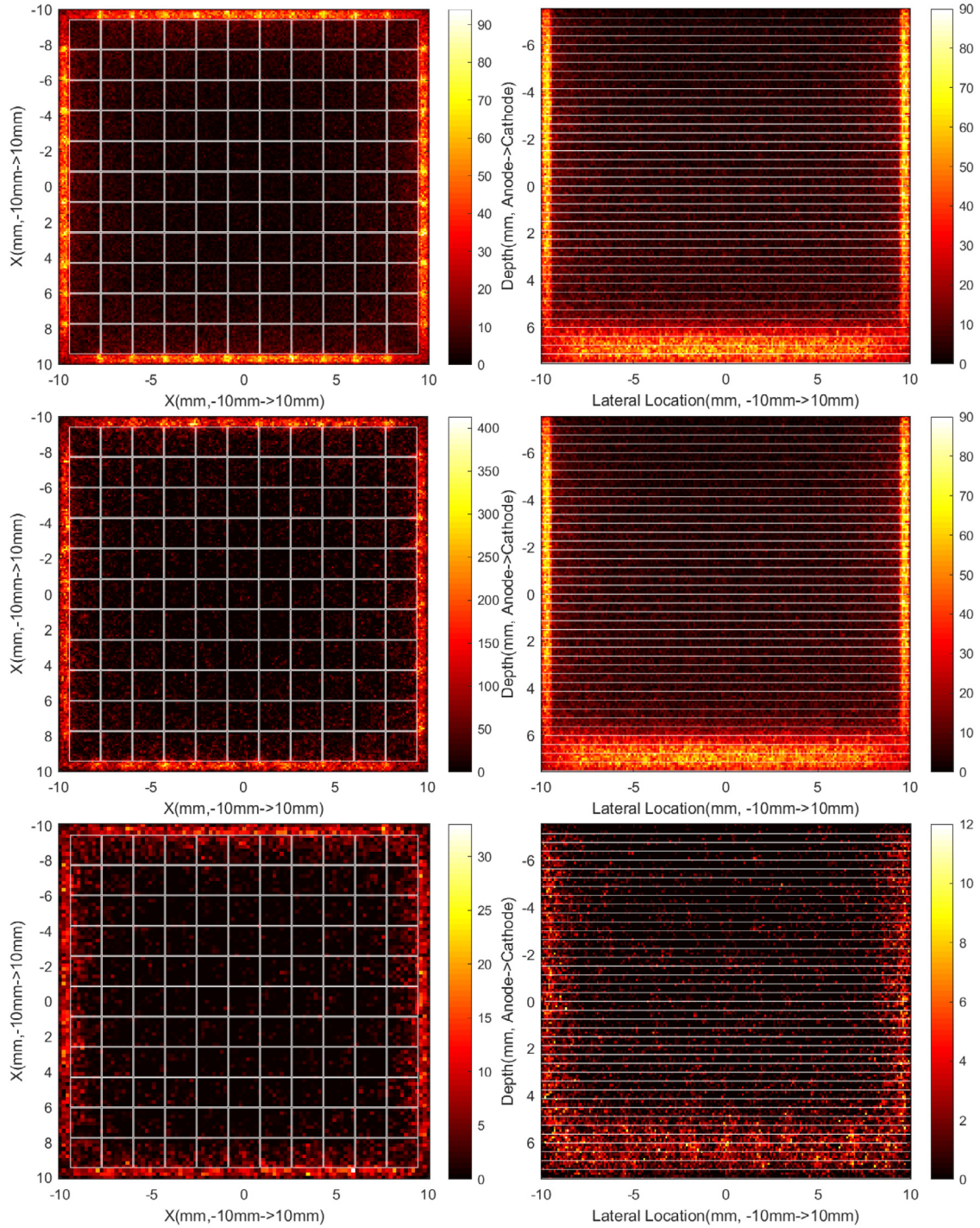
Fig. 15. The location distribution of the lost two-pixel full-energy events from simulation. Top row is at 662 keV. Middle row is at 1274 keV. Bottom row is at 2614 keV. In each row, the lateral position distribution is shown on the left. The pixel grids are marked in white for reference. The cross sectional view of the position distribution is shown on the right. The white lines mark the 40 depth bins.

For three-pixel and four-pixel events, the observation and reasoning remain the same.

5.4. Loss analysis at a given energy

At a given energy, the loss near the anode side becomes more significant as the number of triggered pixels increases. For example, at 661.7 keV, the loss on anode side is 5.79%, 6.15%, 7.02% and 7.86% for 1-pixel, 2-pixel, 3-pixel and 4-pixel events, respectively. The more

interactions one event has, the more likely one or more interactions may happen near the anode side.

Fig. 16 illustrates how the guard ring loss changes as the number of triggered pixels increases. Such trend results from three factors.

First, the electron cloud size increases as energy goes higher. For single pixel events, all of its energy are deposited in one location so the cloud size is the largest. For multi-pixel events, the initial incident energy is deposited at several locations so that each individual cloud size is relatively smaller. Therefore, for multi-pixel events, the effective
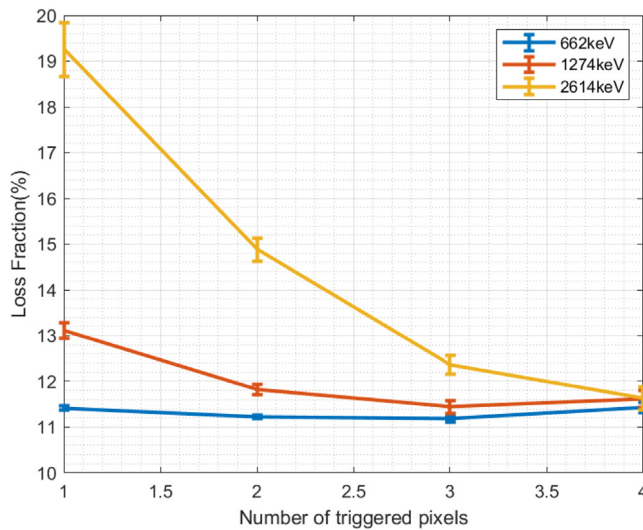
Fig. 16. The significance of guard ring loss for different types of events at different energies.

width of guard ring dead region appears smaller. This factor will decrease the guard ring loss as the number of triggered pixels increases.

Second, the locations of multiple interactions in one radiation event are correlated [12]. At lower energy (e.g. 661.7 keV), the locations of two interactions tend to be close to each other. However, at higher energy (e.g. 2614 keV), the mean distance between interactions in one event is larger, therefore, the two interactions appear more like two independent energy depositions and the loss probability is higher as the interactions spread out more. This factor will increase the guard ring loss as the number of triggered pixels increases.

Third, as number of triggered pixels increases, the initial incident energy are split between several interactions. In this case, even if one interaction falls into the "dead" region under the guard ring or the bad reconstruction layer near the anode, the whole event may still be reconstructed into the photopeak region. For example, if an event with 661.7 keV initial energy deposited 621.7 keV under one pixels and 40 keV under the guard ring, even though the 40 keV events are lost due to the dead region, this event can still be reconstructed into the photopeak region (600–700 keV). This factor will decrease the guard ring loss as the number of triggered pixels increases.

These three factors together caused the observed trend. At 661.7 keV, the second factor is the dominant one, so the loss fractions for different types of events are all around 11%. However, at higher energy like 1274 keV and 2614 keV, the first factor starts to outweigh the other two, so the guard ring loss fraction decreases as the number of triggered pixels increases.

6. Conclusion

Intrinsic photopeak efficiency of pixelated CdZnTe system based on VAD_UM v2.2 digital readout ASIC is studied. The efficiency of a single 20 mm × 20 mm × 15 mm CdZnTe crystal is measured in experiment. The results are summarized in Table 1.

A detailed simulation program that includes the physical process, signal induction and event reconstruction was developed. Efficiency loss mechanisms are identified with the help of this computer program. The simulated and measured intrinsic photopeak efficiency match with each other considering the system uncertainties. Due to the low energy tail of the photopeak that originates from imperfect event reconstruction, the selection of the photopeak region can cause efficiency deficit.

The region under the guard ring is basically "dead" in terms of system response. On the anode side, due to the rapid variation of the weighting potential in one depth bin, the reconstruction of full-energy deposition event may fail and cause efficiency loss.

The efficiency measurement and simulation also provide useful guidance in future radiation detector design. First, to improve the efficiency performance at low energy region, the passive materials between the source and the detector crystal should be minimized. Second, a single larger thicker crystal is preferable, since the region covered by the guard ring and the layer in which weighting potential shows significant variation are relatively smaller. The efficiency loss will be less significant in this case.

CRediT authorship contribution statement

Zhuo Chen: Methodology, Software, Validation, Formal analysis, Investigation, Data curation, Writing - original draft, Visualization. **Yuefeng Zhu:** Methodology, Software, Validation, Formal analysis, Investigation, Writing - review & editing. **Zhong He:** Conceptualization, Writing - review & editing, Supervision, Project administration, Funding acquisition.

Declaration of competing interest

The authors declare that they have no known competing financial interests or personal relationships that could have appeared to influence the work reported in this paper.

Acknowledgments

References

[1] Y. Zhu, M. Streicher, J. Xia, Z. He, Energy resolution improvement and high-energy photon detection in CdZnTe spectrometers with second generation digital electronics and reduced preamplifier trace length, 2018, submitted for publication.

[2] F. Zhang, C. Herman, Z. He, G. De Geronimo, E. Vernon, J. Fried, Characterization of the h3D ASIC readout system and 6.0 cm^3 3-D position sensitive CdZnTe detectors, IEEE Trans. Nucl. Sci. 59 (1) (2012) 236–242.

[3] J. Xia, Interaction reconstruction in digital 3-d cdznte under various circumstances, 2019.

[4] G.F. Knoll, Radiation Detection and Measurement, John Wiley & Sons, 2010.

[5] S. Agostinelli, J. Allison, K.a. Amako, J. Apostolakis, H. Araujo, P. Arce, M. Asai, D. Axen, S. Banerjee, G.. Barrand, et al., GEANT4—a simulation toolkit, Nucl. Instrum. Methods A 506 (3) (2003) 250–303.

[6] J.C. Kim, S.E. Anderson, W. Kaye, F. Zhang, Y. Zhu, S.J. Kaye, Z. He, Charge sharing in common-grid pixelated CdZnTe detectors, Nucl. Instrum. Methods Phys. Res. A 654 (1) (2011) 233–243.

[7] Z. He, Review of the Shockley–Ramo theorem and its application in semiconductor gamma-ray detectors, Nucl. Instrum. Methods Phys. Res. A 463 (1–2) (2001) 250–267.

[8] H. Yang, Applications of digital ASIC array system for noise analysis, non-linearity correction, event classification and reconstruction, 2013.

[9] J. Mann, Improving cadmium zinc telluride spectrometer performance and capabilities, 2016.

[10] F. Zhang, Events reconstruction in 3-d position sensitive cdznte gamma-ray spectrometers, 2005, Citeseer.

[11] Y. Zhu, Digital signal processing methods for pixelated 3-d position sensitive room-temperature semiconductor detectors, 2012.

[12] C.G. Wahl, Imaging, detection, and identification algorithms for position-sensitive gamma-ray detectors, 2011.